Thermochronologic constrains on the processes of formation and exhumation of the Xinli orogenic gold deposit, Jiaodong Peninsula, eastern China

CrossMark

Liang Zhang [a], Li-Qiang Yang [a,*], Yu Wang [a], Roberto F. Weinberg [b], Ping An [a], Bing-Yu Chen [c]

[a] State Key Laboratory of Geological Processes and Mineral Resources, China University of Geosciences, Beijing 100083, China
[b] School of Earth, Atmosphere and Environment, Monash University, Victoria 3800, Australia
[c] Sanshandao Gold Company, Shandong Gold Mining Stock Co., Ltd., Laizhou City, Shandong Province 261442, China

ARTICLE INFO

ABSTRACT

The Xinli orogenic gold deposit, with gold resources of 40 t, located in the northwestern part of the giant Jiaodong gold province, eastern China, is controlled by the Sanshandao Fault and is one of a few deposits hosted by the Early Cretaceous ~129–128 Ma Guojialing granitoid. Soon after intrusion, the granitoid underwent ductile shearing at >400–500 °C marked by recrystallized quartz ribbons and bending of plagioclase lamellae. With rapid cooling from zircon crystallization temperature of ~750–800 °C at ~129–128 Ma (U–Pb) to closure temperature of 300 ± 50 °C for biotite (^{40}Ar/^{39}Ar method) at 124 ± 1 Ma, the ductile deformation lasted <4 million years. Mineralization was associated with subsequent brittle reactivation of normal movement on the fault, indicated by a SE plunging, downdip lineation on the fault. A hydrothermal sericite ^{40}Ar/^{39}Ar age of ~121 Ma, inferred to date the alteration associated with gold mineralization, has been previously obtained for the adjoining Cangshang gold deposit also controlled by the Sanshandao Fault. At the Xinli deposit, the 121.5 ± 1.3 Ma and 120.5 ± 1.2 Ma ^{40}Ar/^{39}Ar plateau ages of weakly-fractured igneous K-feldspar record closely the time of normal faulting and cooling within the range of mineralization temperatures (350–250 °C).

Two zircon fission-track (ZFT) ages of 91 ± 4 Ma and 90 ± 3 Ma constrain the time of cooling through ~240 ± 50 °C. Unimodal distribution of apatite fission-track (AFT) lengths with a slightly negative skew and mean fission-track lengths of 12.3 ± 0.2 μm indicate relative slow continuous cooling through 125–60 °C at 60 ± 6 Ma. The slight acceleration of cooling around ~90 Ma constrained by the ^{40}Ar/^{39}Ar, ZFT and AFT data, and thermal modelling may have resulted from the late normal reactivation of the Sanshandao Fault. In summary, extension and normal faulting not only created the channelways for the mineralizing fluids, but also gave rise to the subdued topography and post-mineralization exhumation that preserved the deposit.

1. Introduction

Thermochronology, such as ^{40}Ar/^{39}Ar and fission-track dating, is widely used to constrain the thermal–tectonic–temporal evolution of the upper crust (Reddy et al., 1999; Reiners and Ehlers, 2005; Wang et al., 2016), and can be further used to reveal the complex processes and dynamic mechanisms underlying this evolution (Reiners et al., 2005). For example, integrated thermochronological methods can reveal the holistic processes of mineralization, hydrothermal alteration and related deformation, as well as the post-mineralization exhumation, and provide new perspectives on mechanisms of ore genesis and

regional exploration targeting (McInnes et al., 2005; Márton et al., 2010; Betsi et al., 2012; Deng et al., 2014; Yang et al., 2016a; Zhang et al., 2016).

Recent contributions of geochronological and thermochronological studies to the literature on the giant Jiaodong gold province (Fig. 1), one of the largest 'gold-only' granitoid-hosted gold province in the world (Li et al., 2015; Phillips and Powell, 2015; Song et al., 2015a; Deng and Wang, 2016), have improved the understanding of this unique gold system (Goldfarb and Santosh, 2014; Yang et al., 2014a; Groves and Santosh, 2016), especially with regards to the timing of crystallization of the igneous rocks hosting the gold (Liu et al., 2014; Yang et al., 2014b; Wang et al., 2014), multi-stage tectonic activity (Charles et al., 2013; Deng et al., 2015a), gold mineralization (Li et al., 2003; Zhang et al., 2003), and post-mineralization exhumation (Liu et al., 2010; Sun et al., 2016). Around the major gold terrane of the Jiaobei Uplift, many zircon U–Pb ages have constrained the emplacement of the

* Corresponding author at: State Key Laboratory of Geological Processes and Mineral Resources, China University of Geosciences, 29# Xue-Yuan Road, Haidian District, Beijing 100083, China.
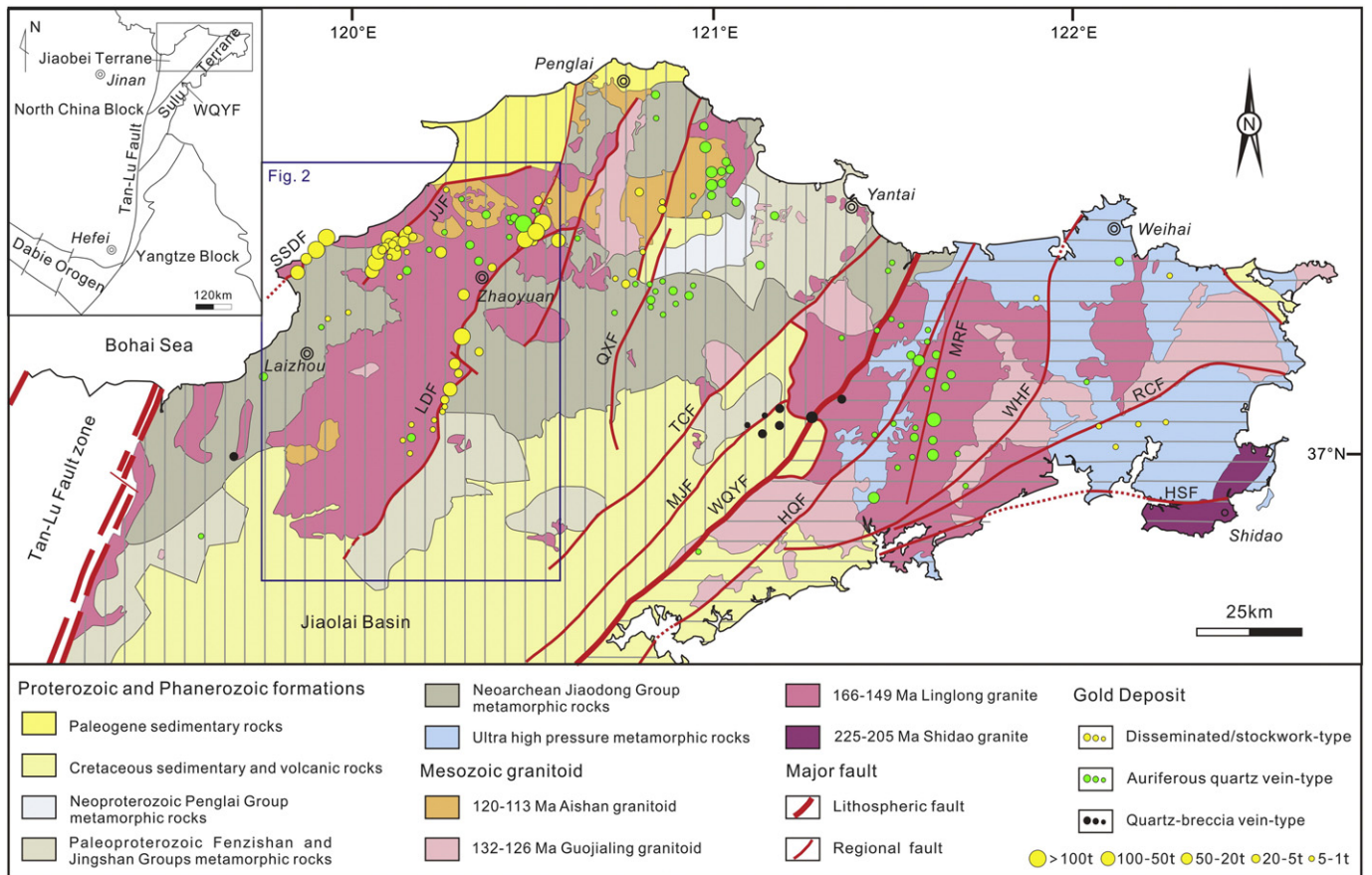 *E-mail address:* lqyang@cugb.edu.cn (L.-Q. Yang).

Fig. 1. Geological sketch map of the Jiaodong Peninsula (modified from Yang et al., 2014a and original map from Wei et al., 2001). HQF, Haiyang–Qingdao Fault; HSF, Haiyang–Shidao Fault; JJF, Jiaojia Fault; LDF, Linglong detachment fault; MJF, Muping–Jimo Fault; MRF, Muping–Rushan Fault; QXF, Qixia Fault; RCF, Rongcheng Fault; SSDF, Sanshandao Fault; TCF, Taocun Fault; WHF, Weihai Fault; WQYF, Wulian–Qingdao–Yantai Fault.

major gold-hosting Linglong- and Guojialing-Type granites to ~166–149 Ma (Yang et al., 2012; Ma et al., 2013) and ~132–126 Ma (Wang et al., 1998; Yang et al., 2012; Wang et al., 2014), respectively. Muscovite $^{40}Ar/^{39}Ar$ ages from a mylonite and brittle fault plane, constrained the timing of ductile and brittle deformation along the Linglong detachment fault at ~134 Ma and ~128 Ma, respectively (Fig. 2a; Charles et al., 2013). In contrast, weak ductile deformation occurred at ~124 Ma (Charles et al., 2013), just before strong overprinting by brittle deformation initiated at ~120 Ma along the Jiaojia Fault (Deng et al., 2015a).

More than 20 high-precision hydrothermal muscovite and sericite $^{40}Ar/^{39}Ar$, and several zircon fission-track (ZFT) ages of gold ores constrain the timing of the major phase of gold mineralization to between 130 and 120 Ma (Fig. 2a; Li et al., 2003; Zhang et al., 2003; Yang et al., 2014c, 2016a, b). In detail, four high-quality $^{40}Ar/^{39}Ar$ and four ZFT ages constrain the early stage of gold mineralization of the Dayingezhuang and Xiadian gold deposits along the Linglong detachment fault to ~130 Ma (Fig. 2a; Yang et al., 2014c, 2016a), while the other $^{40}Ar/^{39}Ar$ ages restrict the age of formation of the Xincheng, Jiaojia and Wanger'shan deposits in the Jiaojia Fault Zone, and the Cangshang deposit along the Sanshandao Fault, to ~120 Ma (Li et al., 2003; Zhang et al., 2003; Yang et al., 2016b). The post-mineralization exhumation of the northwestern part of the Jiaobei Peninsula was estimated at 2–4 km by apatite fission-track (AFT) ages (Liu et al., 2010).

This paper records new thermochronology data from the Xinli gold deposit in the Jiaobei Terrane, part of the Jiaodong gold province. The Xinli gold deposit is a typical disseminated and stockwork-style deposit, with minor auriferous vein-style mineralization, controlled by the Sanshandao Fault, as are the Sanshandao and Cangshang gold deposits (Fig. 2) which are ~1 and ~6 km apart from Xinli deposit, respectively.

All these deposits have essentially the same features: they are all in the footwall of the fault, hosted by granites, and have similar alteration and mineral assemblages. The three deposits are physically linked by continuous low-level alteration and quartz veins along the fault, as shown by drilling.

Several zircon U–Pb ages constrain the crystallization of the host Linglong and Guojialing granites around the deposit to ~166–154 Ma and ~129–128 Ma, respectively (Wang et al., 1998; Zhang et al., 2003; Yang et al., 2012). A sericite $^{40}Ar/^{39}Ar$ age constrains the timing of the gold mineralization at the Cangshang deposit to 121.3 ± 0.4 Ma (Zhang et al., 2003). However, the timing of the gold mineralization and broader cooling history of the Xinli deposit remain to be determined. This study combines field work and previous data with new K-feldspar $^{40}Ar/^{39}Ar$, zircon and apatite fission-track dating, in order to constrain the processes and timing of formation and exhumation of the deposit.

2. Geological background

2.1. Regional geology

The Jiaodong Peninsula lies to the east of the regional Tan–Lu Fault and comprises the Jiaobei and Sulu Terranes (Fig. 1; Deng et al., 2011) that are separated by the Wulian–Yantai–Qingdao Fault. The Jiaobei Terrane comprises the Jiaobei Uplift in the northwest and the Jiaolai Basin in the southeast. The gold deposits of the Jiaobei Uplift account for >85% of the proven gold reserves of the Jiaodong gold province (Qiu et al., 2002). The Jiaobei Uplift mainly comprises the Neoarchean Jiaodong Group of amphibolites and tonalite–
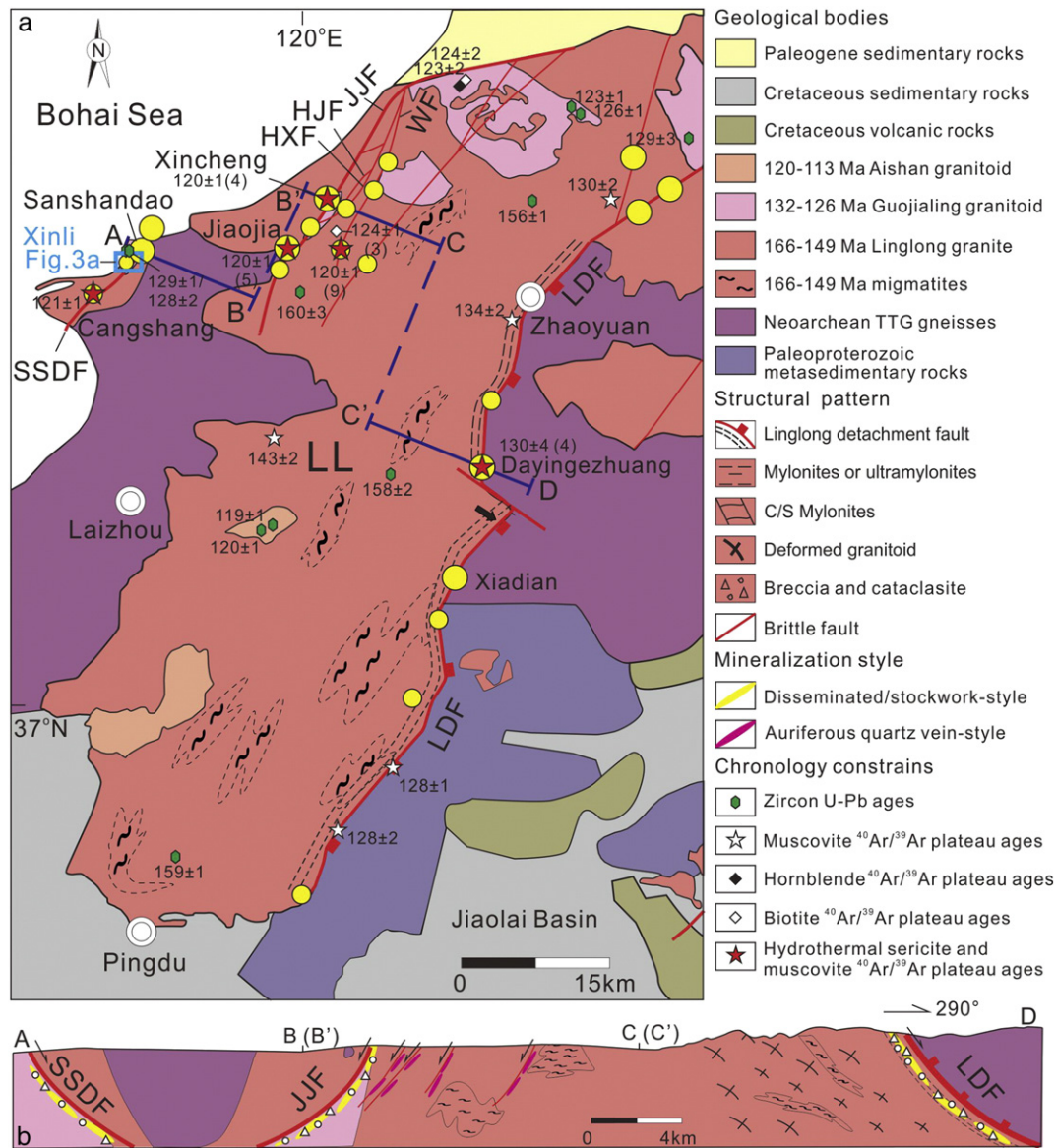
Fig. 2. (a) Geological map of the Jiaobei Uplift and (b) schematic NW–SE section across the Linglong metamorphic core complex (MCC) (modified from: Charles et al., 2011, 2013 and Yang et al., 2016a). Zircon U–Pb ages are from Wang et al. (1998), Li et al. (2012), Yang et al. (2012) and Ma et al. (2013). Hydrothermal muscovite and sericite $^{40}Ar/^{39}Ar$ ages of ores are from Li et al. (2003); Zhang et al. (2003) and Yang et al. (2014c, 2016b). Igneous hornblende, muscovite and biotite $^{40}Ar/^{39}Ar$ ages are from Li et al., (2003), Liu (2010) and Charles et al. (2013). All the marked ages are in Ma. HX, Hexi Fault; HJ, Houjia Fault; JJF, Jiaojia Fault; LDF, Linglong detachment fault; LL, Linglong massif; SSDF, Sanshandao Fault; WES, Wanger'shan Fault. Different size circles represent the tonnages of gold resources for these deposits (>100 t, 100–50 t, <50 t).

trondhjemite–granodiorite (TTG) gneisses, the Paleoproterozoic sedimentary Fenzishan and Jingshan Groups and Mesozoic granites, such as the NE-trending Late Jurassic Linglong granite, Cretaceous ENE-trending Guojialing granitoid, and the late Early Cretaceous (~120–113 Ma; Goss et al., 2010; Li et al., 2012) Aishan-Type granitoid.

Charles et al. (2013) proposed that the Linglong block of granites in this terrane is an asymmetric metamorphic core complex (MCC) bounded by the NNE-trending Linglong detachment fault in the east, where intense and localized ductile deformation marked by mylonites was overprinted by late brittle deformation, hydrothermal alteration and gold mineralization (Fig. 2a, b). To the west of the Linglong detachment fault, the NNE/NE-trending Jiaojia and Sanshandao Faults partly mark the geological boundary between the Mesozoic granites and the older metamorphic rocks, and control the distribution of several super-large gold deposits (Fig. 2a, b). These faults are characterized by intense fracturing with many subsidiary faults, such as the

Wanger'shan, Houjia and Hexi Faults, some of which also host gold deposits (Fig. 2a). The Sanshandao Fault, which controls the Sanshandao (>200 t), Xinli (~40 t) and Cangshang (>50 t) gold deposits, extends north into the Bohai Sea (Fig. 2a) where an offshore resource of >470 t of gold, which is an extension of the Sanshandao orebody (Song et al., 2015b), has been defined by recent exploration.

A synthesis of geological and H–O–C–S–Sr isotopic data suggests that gold mineralization was induced by slab-subduction with ore-forming fluids and metals derived from the dehydration and desulfidation of the subducting paleo-Pacific slab, and the subsequent devolatilization of an enriched mantle wedge (Goldfarb and Santosh, 2014; Deng et al., 2015b). The geological and geochemical data including the structural control of mineralization, lack of any obvious regional zonation of metals and style of mineralization, and the presence of CO_2-rich deep-seated ore-forming fluids (Deng et al., 2015b; Wang et al., 2015) all suggest that most of the deposits including the Xinli gold

deposit, fit the orogenic gold deposit style in the sense of Groves et al. (1998) and Groves and Santosh (2016).

2.2. Ore deposit geology

The Xinli deposit is located in the northwestern part of the Jiaobei Uplift, ~25 km north of Laizhou City (Fig. 2a). In the deposit, the major fault plane of the Sanshandao Fault is marked by a 5–20 cm fault gouge with large striated and grooved surfaces and stretched quartz aggregates plunging consistently SE, indicating normal faulting and NW–SE extension. It separates the barren Archean metamorphic rocks and Linglong granite on the hangingwall, from the gold-hosting Guojialing granitoid on the footwall (Fig. 3a, b). This is one of few deposits hosted by the Guojialing granitoid, which mainly consists of a porphyritic granitoid comprising biotite (Fig. 4a), hornblende, K-feldspar, plagioclase and quartz, with minor magnetite and apatite. The Linglong granite differs in that it is medium-grained but has a similar mineralogy to the Guojialing granitoid, except for little or no hornblende. Most of the Guojialing granitoid underwent ductile shearing, typically localized to recrystallized quartz ribbons, accompanied by gentle bending of plagioclase lamellae (Fig. 4b). Together with strain-induced myrmekite and exsolution of perthite in K-feldspar, the temperature of deformation can be estimated as above 400–500 °C (Passchier and Trouw, 2005).

At the Xinli deposit, a major lens-shaped gold orebody is located in the footwall of the Sanshandao Fault. Gold-related alteration and the lens-shaped orebody are strictly controlled by the Sanshandao Fault and its converging or diverging subsidiary faults. Alteration in the deposit is dominated by sericitization, muscovitization, silicification, pyritization, carbonation and minor chloritization as well as kaolinite alteration. Microscopic observation shows that the altered rocks preserve primary plagioclase and lack newly-formed, non-magmatic K-feldspar. Rocks with intense sericitization, muscovitization, silicification and pyritization define the main orebodies (Fig. 3a–c), while minor auriferous vein-style ores are controlled by subsidiary faults. Away from the main fault plane, alteration is zoned with proximal, intensely (pyrite)–sericite–quartz-altered finely comminuted cataclasite and lenses of breccia, grading to moderately sericite–quartz-altered less-fractured rocks. This is the main ore zone and forms the major lens-shaped orebody reaching 20 m thick, aligned along the fault plane, with gold grades up to 27 g/t and averaging 3 g/t. This alteration phase grades to a distal weak sericite–quartz alteration zone typically marked by its red colouration and inhomogeneous decimeter to meter-scale joints, and finally unaltered rocks cut by widely spaced faults, with limited or no hydrothermal alteration along the cracks. This pattern is similar to that of many deposits in the region such as the Xincheng deposit (Yang et al., 2016c).

Ore minerals include pyrite, chalcopyrite, galena, sphalerite and minor arsenopyrite. There are four stages of hydrothermal alteration and mineralization (Fig. 5). Stage 1 alteration involved the initial breakdown of mafic minerals to chlorite, and then to fine-grained sericite and quartz, as well as minor coarse-grained muscovite. At this stage, minor pyrite (Py_1) was deposited. Feldspar then started to break down to fine-grained sericite, coarse-grained muscovite and quartz (Fig. 4c). In stage 2, voluminous coarse-grained pyrite with quartz formed with minor gold (Py_2; Fig. 4e, f). Following their formation, in stage 3 many pyrite grains were fractured, with gold, late very fine-grained pyrite (Py_3) overgrowing Py2, and base-metal sulfides (Fig. 4f) such as chalcopyrite, galena, sphalerite and minor arsenopyrite found in the fractures (Fig. 4f, g). Sericite/muscovite and quartz continued to be deposited during the first three stages with variable intensity (Figs. 4c–e and 5). Finally, at stage 4, termination of mineralization and alteration was marked by the occurrence of late-forming (quartz)–carbonate (Fig. 4h), producing features such as (quartz)–calcite veins.

The estimated lower limit of ore-forming temperatures reported for the main orebodies in the gold deposit, based on fluid-inclusion microthermometry, is ~330–180 °C with a wide range of 369–116 °C (Pan, 2013; Deng et al., 2015b). Based on the hydrothermal mineral assemblage of sericite, muscovite, quartz, chlorite and pyrite (Fig. 4), and syn-mineralization brittle deformation, the ore-forming temperature is inferred to be 300 ± 50 °C.
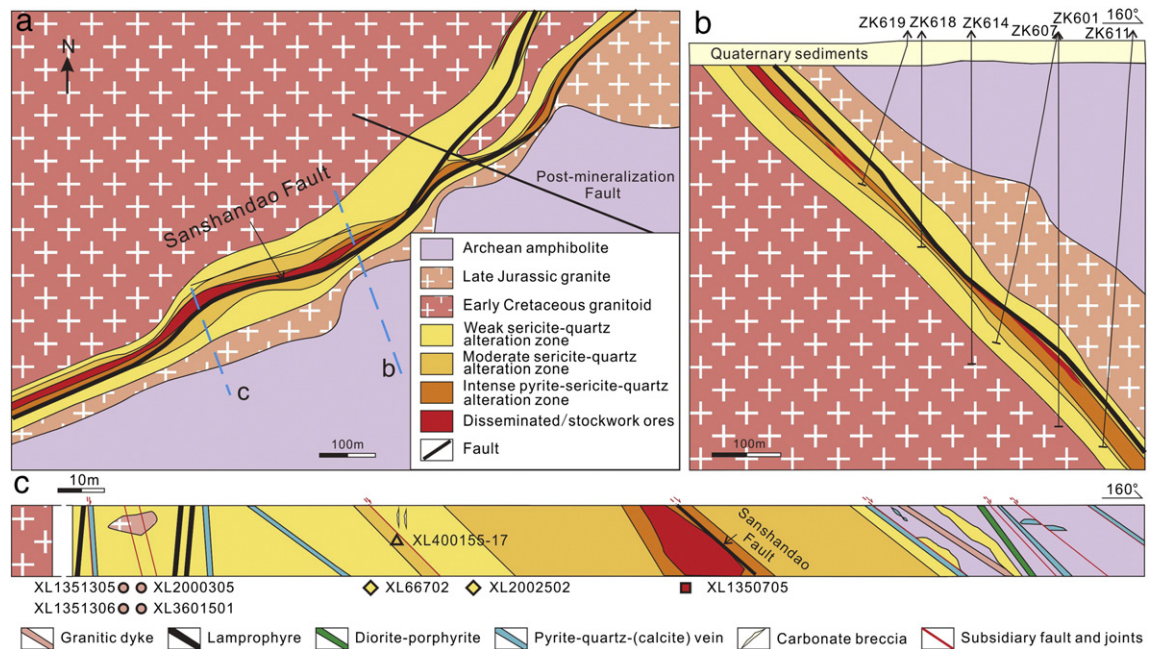

Fig. 3. (a) Geological map of the Xinli gold deposit; (b) cross-section showing alteration halos; and (c) cross-section at −400 m level showing the alteration halos, structures and sample locations; Samples XL1351305, XL1351306, XL3601501, XL66702, XL2000305, XL2002502 and XL1350705 were not taken from this cross-section but listed to show relative locations of the samples in different alteration zones. Sample symbols in (c): pink circle, unaltered to weak altered porphyritic Guojialing granitoid; yellow diamond, weak sericite–quartz-altered granitoid; dark yellow triangle, sericite–quartz-altered breccia; red square, intensely pyrite–sericite–quartz-altered breccia ore. The colour of the symbols refers to the alteration zones.
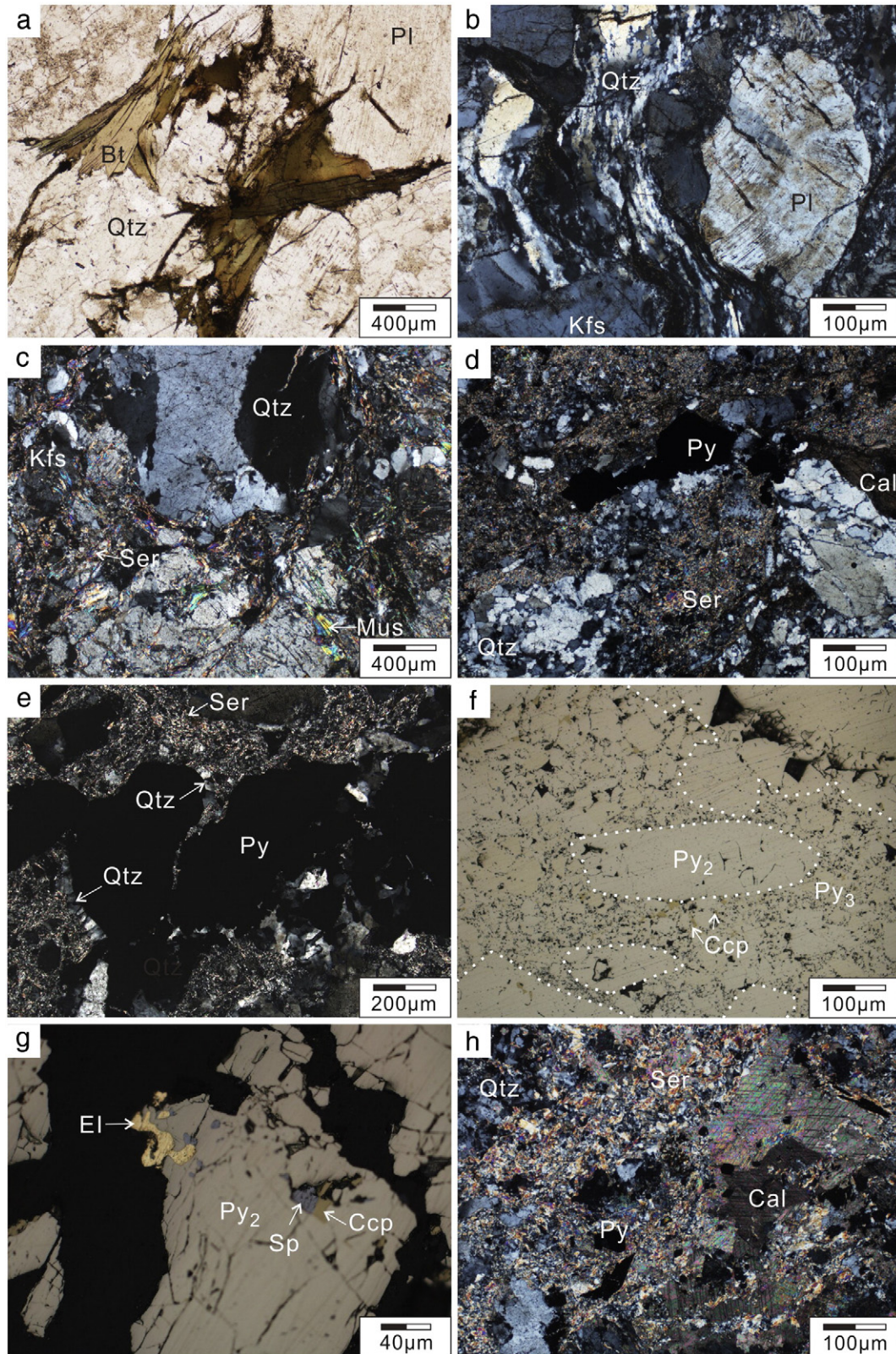
Fig. 4. Photomicrographs showing features of mineralogy, texture, alteration and deformation. (a, b) photomicrographs of Guojialing granitoid; (a) unaltered biotite in sample XL1351305; (b) recrystallized quartz ribbons and bending of plagioclase lamellae typical of Guojialing granite and recognizable across the terrane; (c) first step of breakdown of K-feldspar forming fine-grained sericite and muscovite in samples from weak sericite–quartz alteration zone; (d–h) photomicrographs of samples from intense pyrite–sericite–quartz alteration zone; (d) pyrite–sericite–quartz alteration with residual recrystallized igneous quartz; (e) fibrous hydrothermal quartz developed in pressure shadows on edges of pyrite at stage 2; (f) brecciated and fractured pyrite formed at stage 2 (Py_2) with late pyrite (Py_3) and chalcopyrite as cement between Py_2 clasts and filling in cracks inside grains; (g) sphalerite, chalcopyrite and electrum in fractures in pyrite; (h) intensely altered ore rock (sericite, silica, sulfides) with late calcite (stage 4) including sericite grains. Bt, biotite; Cal, calcite; Ccp, chalcopyrite; El, electrum; Kfs, K-feldspar; Mus, muscovite; Qtz, quartz; Pl, plagioclase; Py, pyrite; Ser, sericite; Sp, sphalerite. (a) plane-polarized light; (b–e, h) crossed-polarized light; (f, g) reflected light.
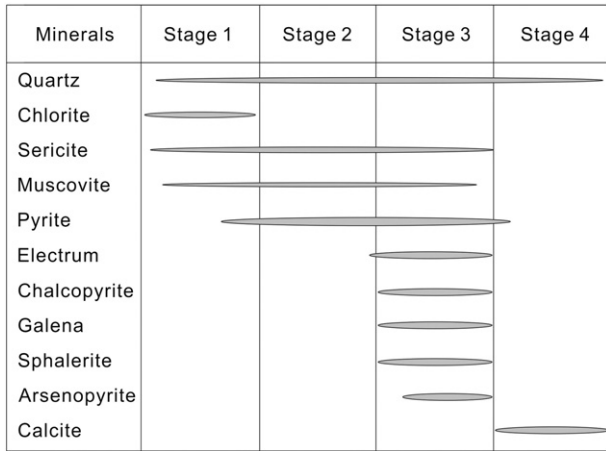
Fig. 5. Paragenetic sequence of hydrothermal minerals at the Xinli gold deposit. Relative abundance of minerals is represented by the width of the solid lines.

3. Thermochronology

3.1. Sample selection and description

A total of eight samples of typical host rocks and ore samples were obtained for thermochronology at different mining levels from −135 m to −667 m on the footwall of the Sanshandao Fault (Table 1; Fig. 3c). These include four Guojialing granitoid samples, two moderately sericite–quartz-altered granitoid, one sericite–quartz-altered breccia, and one intensely pyrite–sericite–quartz-altered breccia ore sample.

The Guojialing granitoid samples XL1351305, XL1351306, XL2000305 and XL3601501 were very weakly deformed with quartz showing dynamic recrystallization and many micro-fractures cutting through feldspar grains. Biotite has minor chlorite alteration, although most biotite grains are unaltered (Fig. 4a). Some K-feldspar and plagioclase show weak sericite–kaolinite alteration (Fig. 6a, b).

Samples XL2002502 and XL66702 show plastic deformation recorded by recrystallized quartz grains, and were overprinted by late hydrothermal alteration and fracturing. Many micro-fractures cross cut the feldspar grains. Many K-feldspar grains have been partly altered to sericite and quartz while some are preserved (Fig. 6c, d). In general, plagioclase has more intense sericite–quartz alteration than K-feldspar (Fig. 6c, d), especially grains included in K-feldspar.

The breccia ore sample XL1350705 and low-grade sericite–quartz-altered breccia sample XL400155-17 show intense sericite–quartz alteration and fracturing. Most of the primary minerals have been altered

with some residual recrystallized quartz (Fig. 4d) and minor K-feldspar with irregular shape.

In this paper we report on $^{40}Ar/^{39}Ar$ dating of unaltered biotite (Fig. 4a) and weakly fractured K-feldspar (Fig. 6a) from sample XL1351305, fresh weakly fractured K-feldspar (Fig. 6b) from sample XL3601501, and fractured K-feldspar (Fig. 6c, d) from sample XL66702. Zircon grains from samples XL2002502 and XL400155-17, and apatite grains from samples XL1351306, XL1350705 and XL2000305 were used for fission-track dating (Table 1).

3.2. Methods

3.2.1. $^{40}Ar/^{39}Ar$ step-heating dating

Biotite and K-feldspar grains for $^{40}Ar/^{39}Ar$ dating were handpicked to 99% purity after crushing using a jaw crusher and a disk mill. After cleaning with distilled water and acetone, and drying at 50 °C, the separates and the standard mineral Fish Canyon Tuff (FCT) sanidine with an age of 27.55 ± 0.08 Ma (Lanphere and Baadsgaard, 2001) and ZBH-25 biotite, with a $^{40}Ar/^{39}Ar$ age of 132.7 ± 0.2 Ma and potassium content of 7.6% (Wang, 1983; Fu et al., 1987), were sent to the China Institution of Atomic Energy in Beijing for fast neutron radiation. The samples and standards were set in the H8 hole, and the irradiation duration and neutron dose were 10.7 h and 2.45×10^{17} n/cm². The J factor was estimated by replicate analysis of FCT sanidine. The Ca and K correction factors calculated from co-irradiation of pure salts of CaF_2 and K_2SO_4 are $(^{40}Ar/^{39}Ar)_K = 0.004782$, $(^{39}Ar/^{37}Ar)_{Ca} = 0.00081$, and $(^{36}Ar/^{37}Ar)_{Ca} = 0.0002398$. At the China University of Geosciences, Beijing, samples were incrementally heated in a double-vacuum furnace, and $^{40}Ar/^{39}Ar$ analyses were performed on a MM-5400 Micromass spectrometer operating in a static mode following the experimental method of Wang and Li (2008). Argon isotopic results were corrected for system blanks, mass discrimination, radioactive decay, reactor-induced interference reactions and atmospheric argon contamination; Steiger and Jäger's (1977) decay constant [$\lambda = (5.543 \pm 0.010) \times 10^{-10}$ a^{-1}] was used. Dates and errors were calculated using the software from the Berkeley Geochronological Center, while plateau ages in 2σ level were calculated using ISOPLOT version 4.16 (Ludwig, 2012).

3.2.2. Fission-track dating and thermal modelling

Zircon and apatite grains were separated using traditional heavy-liquid techniques. Fission-track dating was performed at the Institute of High Energy Physics of the Chinese Academy of Sciences (IHEPCAS) using the external detector method (Gleadow, 1981). Zircon and apatite crystals without fractures and fluid inclusions were selected for dating. Zircon grains were etched in a KOH–NaOH eutectic at 220 °C for 25 h, while apatite grains were etched in 5.0% HNO_3 for 20 s at 20 °C. Radiation was then performed on a hot-neutron nuclear reactor at the China Institution of Atomic Energy, Beijing, with Corning CN5 and CN2

Table 1
Sample description of the Xinli deposit.

| Sample number	Location	Rock type	Elevation (m)	Minerals for dating	
				$^{40}Ar/^{39}Ar$	Fission-track
XL1351305	Weak sericite-quartz alteration zone	Unaltered to weakly altered porphyritic Guojialing granitoid	−135	Biotite, K-feldspar	/
XL3601501	Weak sericite-quartz alteration zone	Unaltered to weakly altered porphyritic Guojialing granitoid	−360	K-feldspar	/
XL66702	Weak sericite-quartz alteration zone	Weakly sericite-quartz altered granitoid	−667	K-feldspar	
XL2000305	Weak sericite-quartz alteration zone	Unaltered to weakly altered porphyritic Guojialing granitoid	−200	/	Apatite
XL1351306	Weak sericite -quartz alteration zone	Unaltered to weakly altered porphyritic Guojialing granitoid	−135	/	Apatite
XL2002502	Weak sericite -quartz alteration zone	Weakly sericite-quartz altered granitoid	−200	/	Zircon
XL400155-17	Medium sericite–quartz alteration zone	Sericite–quartz altered breccia	−400	/	Zircon
XL1350705	Intense pyrite-sericite–quartz alteration zone (Ore zone)	Intensely pyrite-sericite–quartz altered breccia ore	−135	/	Apatite
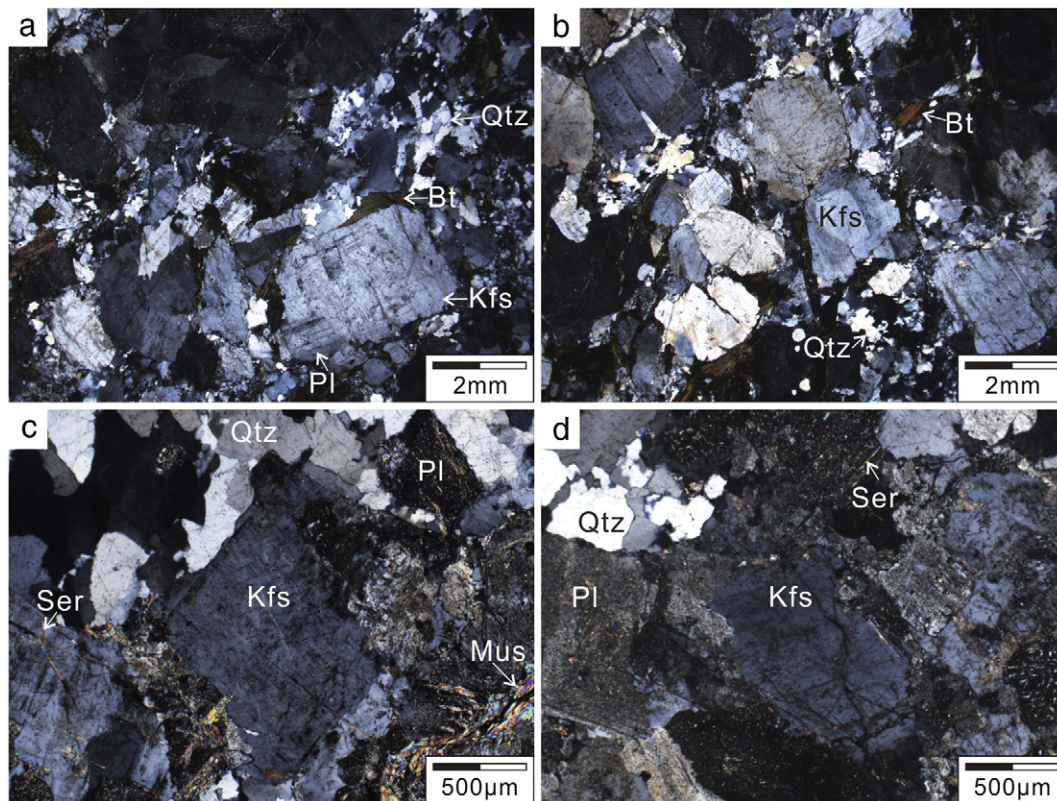
Fig. 6. Crossed-polarized light photomicrographs showing features of K-feldspar in samples used for ^{40}Ar/^{39}Ar dating. Weakly fractured igneous, subhedral K-feldspar in samples XL1351305 (a) and XL3601501 (b); (c, d) fractured K-feldspar in sample XL66702; some plagioclase grains have been strongly sericitized. Bt, biotite; Kfs, K-feldspar; Mus, muscovite; Qtz, quartz; Pl, plagioclase; Ser, sericite.

uranium dosimeter glasses as the monitor of neutron effluence for AFT and ZFT dating (Yuan et al., 2009), respectively. Later, 40% HF was used to reveal the induced fission-tracks on the low-uranium muscovite external detectors at room temperature for 20 min. The track densities in both natural (ρ_s) tested grains, and induced (ρ_i) fission-track populations in the muscovite external detectors, as well as the induced track densities of dosimeter glasses (ρ_d), were measured at 1000× magnification on screen photos. Confined apatite fission-track lengths parallel to the C-axis were measured. The uranium contents are estimated based on the induced fission-track densities on the low-uranium muscovite external detectors.

Central ages were calculated using RadialPlotter software (Vermeesch, 2009) and the Zeta calibration method (Hurford and Green, 1983), with a zeta value of 85.4 ± 4.0 for CN2 for zircon and 389.4 ± 19.2 for CN5 for apatite. A chi-square (χ^2) test (Galbraith, 1981) was performed to estimate whether the single grain ages belong to the same age population. Generally, the apparent fission-track ages represent the time that samples cooled through the closure temperature (~240 ± 50 °C for zircon; Zaun and Wagner, 1985; Hurford, 1986; Bernet, 2009; ~100 ± 20 °C for apatite; Wagner and Haute, 1992). However, for samples that cooled slowly, the AFT age may represent the time that the samples cooled through the partial annealing zone (PAZ, 125–60 °C; Gleadow and Duddy, 1981), in which case the fission-track length should be relative short.

Inverse thermal modelling for sample XL1351306 with enough measured confined tracks (≥100) was undertaken based on the annealing model of Ketcham et al. (2007) using HeFTy software (Ketcham, 2012) with the Monte Carlo method. Constraints used for modelling are: (a) Present-day temperature of 25 ± 5 °C; (b) PAZ of AFT method at a time-span wider than the corresponding AFT age; and (c) closure temperature of ZFT and biotite ^{40}Ar/^{39}Ar

method, and corresponding ages. One hundred acceptable paths were obtained for the inverse thermal history model. Given no kinetic parameters were obtained, the kinetic parameter Dpar of ~1.5 obtained from the same rocks in the northwestern part of the Jiaodong Peninsula, which also have been tested at the IHEPCAS following the same processes (Wang et al., 2016 Personal communication), was used in the thermal modelling.

3.3. Results and interpretation

3.3.1. Biotite and K-feldspar ^{40}Ar/^{39}Ar ages

Unaltered biotite grains from sample XL1351305 yielded a well-defined ^{40}Ar/^{39}Ar plateau age of 124.2 ± 1.0 Ma using 99.98% ^{39}Ar released (Table 2; Fig. 7). The plateau age is consistent with its isochron age of 125.0 ± 0.5 Ma within error. Its ^{40}Ar/^{36}Ar intercept of 289.7 ± 2.4 indicates the biotite grains contain no excess argon. Therefore, the biotite ^{40}Ar/^{39}Ar plateau age is taken to represent the time the sample cooled through its closure temperature of ~300 ± 50 °C (McDougall and Harrison, 1999).

Weakly fractured K-feldspar from the same sample yielded a little younger ^{40}Ar/^{39}Ar plateau age of 121.5 ± 1.3 Ma using 72.8% ^{39}Ar released (Table 2; Fig. 7), while weakly fractured K-feldspar in the unaltered to weakly altered Guojialing granitoid sample XL3601501 yielded a similar ^{40}Ar/^{39}Ar plateau age (120.5 ± 1.2 Ma) using 62.3% ^{39}Ar released (Table 2; Fig. 7). Their ^{40}Ar/^{36}Ar intercepts of 303 ± 29 and 289 ± 22, respectively are in line with the atmospheric ratio of 295.5 ± 0.5 (Nier, 1950), indicating no significant argon loss or excess argon. The well-defined flat age spectrum of these two samples is different from the complex staircase-shaped age spectra expected for igneous K-feldspar (McDougall and Harrison, 1999) from granites. This may be caused by rapid cooling or resetting (Forster and Lister, 2004). In view

Table 2
^{40}Ar/^{39}Ar step-heating data for samples from Xinli deposit.

Temp (°C)	$(^{40}Ar/^{39}Ar)_m$	$(^{36}Ar/^{39}Ar)_m$	$(^{37}Ar/^{39}Ar)_m$	$(^{40}Ar_a/^{39}Ar_k)_m$	^{39}Ar ($\times 10^{-8}$ ccSTP)	^{39}Ar (%)	$^{40}Ar_a$	Age (Ma)	Error (1σ, Ma)
Sample number = XL1351305; mineral = biotite; wt. = 0.02764 g; J = 0.002232.									
730	89.694	0.187	1.955	34.645	0.002	0.02	39.37	134.37	58.68
830	292.546	0.888	4.703	30.734	0.002	0.02	11.64	119.69	232.34
930	161.195	0.470	0.401	22.303	0.021	0.19	14.96	87.64	14.20
980	70.437	0.132	0.060	31.287	0.466	4.30	45.14	121.77	1.77
1030	47.598	0.053	0.013	32.058	0.614	5.67	67.78	124.67	1.73
1070	34.289	0.007	0.008	32.170	1.854	17.12	93.90	125.09	1.72
1100	32.989	0.003	0.006	32.130	2.015	18.60	97.43	124.95	1.71
1140	32.972	0.003	0.007	32.158	1.815	16.76	97.56	125.05	1.71
1190	34.083	0.007	0.018	32.031	0.822	7.59	94.06	124.57	1.73
1240	35.156	0.012	0.035	31.723	0.453	4.19	90.36	123.41	1.77
1300	35.776	0.013	0.020	31.852	0.406	3.75	89.17	123.90	1.35
1350	34.218	0.007	0.010	32.003	1.160	10.71	93.61	124.47	1.22
1400	34.430	0.008	0.011	31.954	1.200	11.08	92.90	124.28	1.21
Sample number = XL1351305; mineral = K-feldspar; wt. = 0.04030 g; J = 0.002201.									
730	1065.714	3.056	7.868	164.234	0.002	0.03	16.42	556.66	613.29
830	502.704	1.653	1.097	14.309	0.007	0.12	4.11	55.94	87.50
930	96.271	0.230	0.115	28.273	0.057	1.01	30.29	108.91	3.72
980	44.668	0.044	0.059	31.523	0.094	1.66	70.95	121.01	3.04
1030	39.425	0.031	0.026	30.265	0.450	7.88	77.07	116.34	1.72
1070	34.382	0.012	0.006	30.775	0.419	7.33	89.64	118.23	1.69
1130	34.769	0.014	0.008	30.718	0.523	9.16	88.50	118.02	1.68
1170	37.315	0.021	0.011	31.222	0.337	5.90	83.88	119.90	1.78
1210	38.034	0.022	0.007	31.484	0.361	6.32	83.00	120.87	1.75
1250	39.849	0.028	0.018	31.428	0.325	5.69	79.14	120.66	1.72
1300	40.991	0.032	0.011	31.472	0.620	10.85	77.08	120.82	1.23
1350	40.601	0.030	0.010	31.739	0.962	16.86	78.46	121.82	2.13
1400	39.037	0.023	0.002	32.181	1.552	27.18	82.67	123.45	1.20
Sample number = XL3601501; mineral = K-feldspar; wt. = 0.04320 g; J = 0.002239.									
730	413.229	1.339	1.130	17.759	0.007	0.15	5.54	70.34	64.78
830	327.728	1.006	0.583	30.402	0.005	0.10	10.46	118.80	88.95
930	79.363	0.188	0.144	23.942	0.072	1.50	31.08	94.20	4.05
980	54.174	0.089	0.120	27.795	0.238	4.92	51.94	108.91	1.61
1030	55.628	0.087	0.018	29.973	0.246	5.07	54.48	117.17	1.93
1070	34.851	0.017	0.079	29.759	0.270	5.58	85.58	116.37	1.74
1100	32.907	0.010	0.054	29.937	0.346	7.14	91.09	117.04	1.72
1140	33.470	0.011	0.008	30.227	0.273	5.64	90.44	118.14	1.74
1180	34.847	0.015	0.019	30.362	0.366	7.57	87.30	118.65	1.68
1220	35.576	0.017	0.005	30.602	0.334	6.91	86.20	119.56	1.75
1260	36.789	0.021	0.020	30.685	0.323	6.67	83.62	119.87	1.52
1300	37.337	0.023	0.021	30.600	0.417	8.62	82.19	119.55	1.24
1350	37.070	0.021	0.008	30.805	0.745	15.38	83.32	120.32	1.22
1400	36.610	0.018	0.000	31.364	1.199	24.76	85.86	122.43	1.18
Sample number = XL66702; mineral = K-feldspar; wt. = 0.04030 g; J = 0.002194.									
730	276.736	0.128	6.372	240.742	0.105	1.14	86.72	765.05	37.34
830	454.481	0.737	6.789	238.606	0.028	0.31	52.84	759.50	63.04
930	60.964	0.131	0.247	22.225	0.475	5.16	37.28	85.89	1.38
980	58.387	0.105	0.129	27.284	0.506	5.49	47.42	104.88	1.78
1030	53.932	0.083	0.105	29.390	0.327	3.55	55.08	112.73	1.70
1070	43.662	0.046	0.027	30.061	0.660	7.16	69.26	115.22	1.60
1100	47.643	0.059	0.032	30.060	0.404	4.39	63.57	115.22	1.63
1140	44.129	0.047	0.029	30.283	0.442	4.80	69.03	116.05	1.65
1180	43.894	0.046	0.041	30.217	0.638	6.92	69.24	115.80	1.62
1220	47.805	0.060	0.262	30.001	0.556	6.03	63.23	115.00	1.94
1260	45.686	0.050	0.040	30.798	0.597	6.48	67.84	117.96	1.22
1300	43.943	0.045	0.045	30.550	0.944	10.25	69.92	117.04	1.19
1350	38.736	0.027	0.006	30.805	1.411	15.32	79.79	117.98	1.16
1400	37.534	0.020	0.000	31.616	2.117	22.99	84.44	120.99	1.17

of the fracturing of the K-feldspar grains, it is suggested that the flat age spectra may result from the rapid resetting of the argon system by fracturing during normal faulting (Wang and Zhou, 2009), while rapid cooling is ruled out by the constraints from biotite ^{40}Ar/^{39}Ar age of 124.2 ± 1.0 Ma and ZFT ages (see below), and their closure temperatures.

Fractured K-feldspar from the moderately sericite–quartz-altered sample XL66702 yielded an ^{40}Ar/^{39}Ar plateau age of 116.7 ± 1.0 Ma (Table 2; Fig. 7), younger than the isochron age of 121.6 ± 2.6 Ma, and also younger than the unaltered to weakly altered samples. The ^{40}Ar/^{36}Ar intercept of 264 ± 5 is lower than that of the atmospheric

ratio of 295.5, showing that, unlike the other samples, this sample underwent significant argon loss. In this case, the plateau age of 116.7 ± 1.0 Ma is meaningless, while the isochron age of 121.6 ± 2.6 Ma may roughly represent the original cooling/reset age of the sample (McDougall and Harrison, 1999) although it may give a "mixed age". Conservatively, neither the plateau nor the isochron ages of this sample will be used for further discussion.

The well-defined ~121 Ma K-feldspar ^{40}Ar/^{39}Ar plateau ages of samples XL1351305 and XL3601501 lie between that of the biotite (124.2 ± 1.0 Ma) and that of ZFT dating (see below), which is consistent with the intermediate K-feldspar closure temperature.
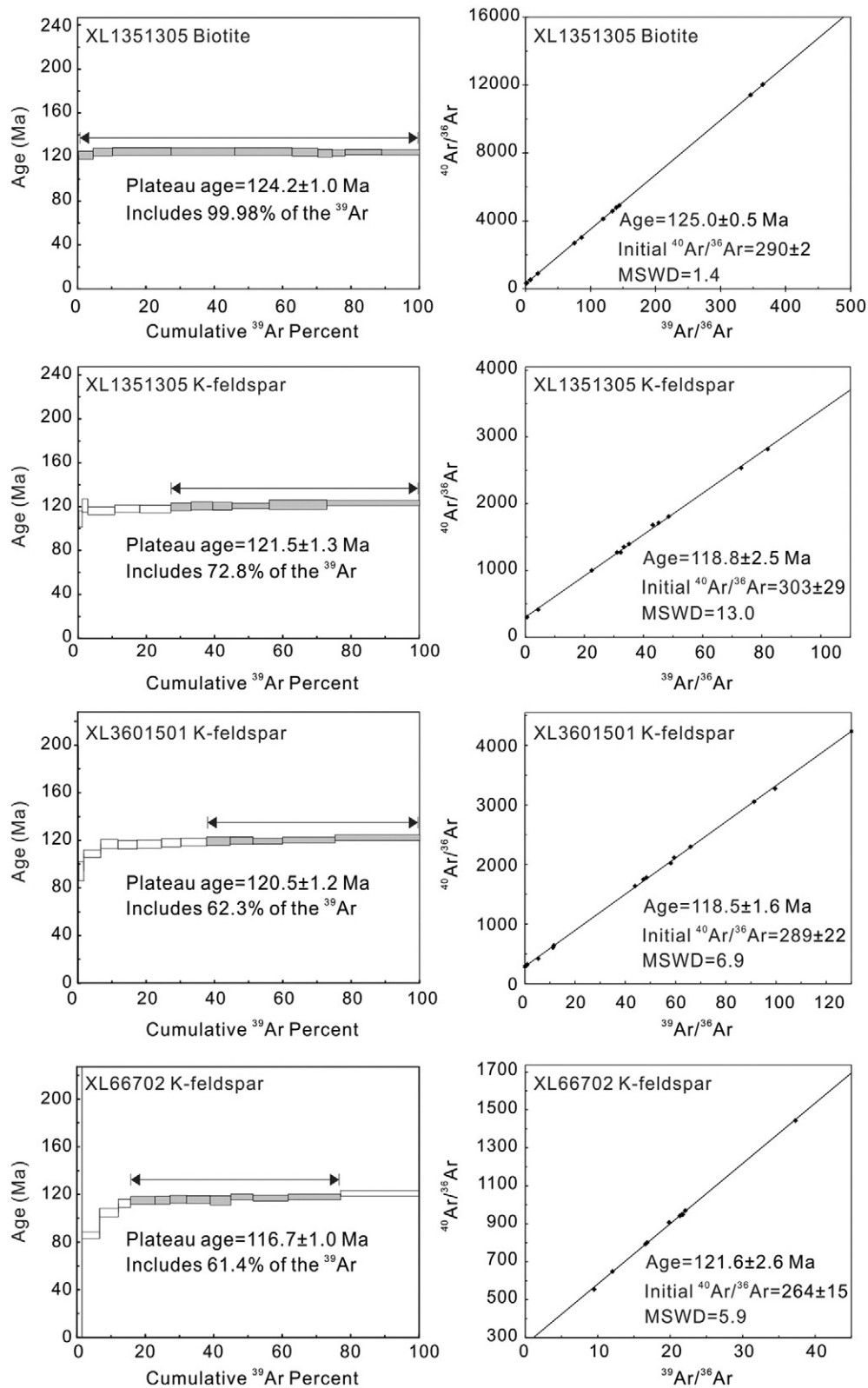
Fig. 7. ^{40}Ar/^{39}Ar plateau and isochron ages (2σ) for biotite and K-feldspar from the Xinli deposit.

3.3.2. Zircon fission-track ages

Samples XL2002502 and XL400155-17 yielded ZFT ages of 90.5 ± 3.8 Ma and 89.8 ± 3.1 Ma, with single grain ages of ~140.2 ± 30.0– 66.3 ± 8.6 Ma and ~124.7 ± 35.7–70.9 ± 12.3 Ma, respectively (Table 3; Fig. 8). Sample XL2002502 failed the P(χ^2) test. Given the granite

protolith of the samples, and the consistent zircon U–Pb ages for these rocks (Wang et al., 1998; Liu et al., 2014; Wang et al., 2014), the possibility of different sources for the zircons can be ruled out. Furthermore, the relative low uranium content of the zircons (<350 ppm, Fig. 8) suggests that the spread of ages cannot be a result of significant radiation

Table 3
Zircon fission-track data. Induced track densities on dosimeter glasses and mica external detectors as well as spontaneous track density on internal mineral surfaces are represented by ρ_d, ρ_i and ρ_s, respectively, while N_d, N_i and N_s are the number of tracks on monitor glasses, external detectors and mineral surfaces. $P(\chi^2)$ values lower than 5% are considered to fail the chi-square probability test (Galbraith, 1981).

Sample number	Elevation (m)	Number of grains	ρ_d (N_d) ($\times 10^5$ cm^{-2})	ρ_s (N_s) ($\times 10^5$ cm^{-2})	ρ_i (N_i) ($\times 10^5$ cm^{-2})	Uranium content (ppm)	$P(\chi^2)$ (%)	Central Age (1σ, Ma)
XL2002502	−200	28	5.533 (4630)	116.989 (5957)	30.283 (1542)	212	0	90.5 ± 3.8
XL400155-17	−400	22	5.600 (4630)	153.355 (4432)	40.450 (1169)	258	44	89.8 ± 3.1

damage. Therefore, the low $P(\chi^2)$ value probably results from introduced errors such as poor etching of particular grains (Yang et al., 2016a). In this case, a small number of poor single grain ages have no obvious influence on the central ages (Galbraith, 1984). Therefore, the two consistent ZFT ages of 90.5 ± 3.8 Ma and 89.8 ± 3.1 Ma represent the time the samples cooled through ~240 ± 50 °C (Zaun and Wagner, 1985; Hurford, 1986; Bernet, 2009).

3.3.3. Apatite fission-track data and thermal modelling

Three samples from −135 m and −200 m depth, including ores and unaltered wall rocks, yielded AFT ages of 61.8 ± 3.5 Ma, 59.8 ± 6.3 Ma, and 58.7 ± 2.5 Ma (Table 4; Fig. 9). All samples passed the $P(\chi^2)$ test, showing that single-grain ages in each sample belong to the same age group. Fission-track length was measured for all three samples, although only sample XL1351306 yielded robust length data with 112 counted tracks (Fig. 10). In this sample, the unimodal distribution of the AFT lengths with slightly negative skewness (Fig. 10) and mean fission-track length of 12.3 ± 0.2 µm indicate relative slow continuous cooling through the apatite PAZ 125–60 °C (Gleadow and Duddy, 1981).

The modelled cooling history of sample XL1351306 (Fig. 10) indicates three main cooling stages: ~125–90 Ma, ~90–70 Ma, and ~70-

present and indicate that the Xinli deposit cooled slowly, except for relative fast cooling at ~90–70 Ma.

4. Discussion

4.1. Timing and structural controls on gold mineralization

Along with regional extension (Charles et al., 2013; Yang et al., 2016a), lithospheric thinning and destabilization of the North China Craton (Wu et al., 2008), the Guojialing granitoid intruded at ~129–128 Ma (Figs. 10 and 11a; Wang et al., 1998; Yang et al., 2012), with estimated magma temperatures of ~750–800 °C (Zhang et al., 2010). Soon after intrusion, the Guojialing granitoid underwent ductile shearing (Fig. 4b) that probably continued through cooling to temperatures of 400–500 °C. ^{40}Ar/^{39}Ar age of undeformed biotite of 124.2 ± 1.0 Ma constrains the time of the granitoid cooling through 300 ± 50 °C (McDougall and Harrison, 1999) and possibly post-dates most of the ductile shearing, because the lower closure temperature of biotite for Ar diffusion than the ductile deformation temperatures of the granites. This suggests that rapid cooling from magmatic temperatures related
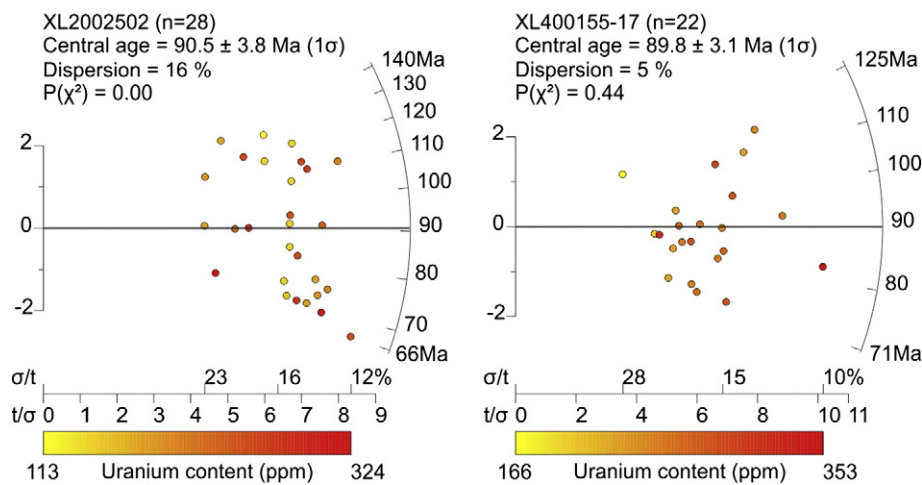

XL2002502 (n=28)
Central age = 90.5 ± 3.8 Ma (1σ)
Dispersion = 16 %
$P(\chi^2)$ = 0.00

XL400155-17 (n=22)
Central age = 89.8 ± 3.1 Ma (1σ)
Dispersion = 5 %
$P(\chi^2)$ = 0.44

Fig. 8. Radial plots of zircon fission-track samples. Single-grain ages are defined by the intersection between a line linking the origin with the single-grain point and the arc. Y-axis represents standard error of each measurement. The central ZFT ages (Table 3) are shown by continuous and nearly horizontal lines. The colour of the single-grain point represents the uranium content of single zircon grains.

Table 4
Apatite fission-track data. Length in the table means average length of measured fission-tracks. Other parameters are the same as in Table 3.

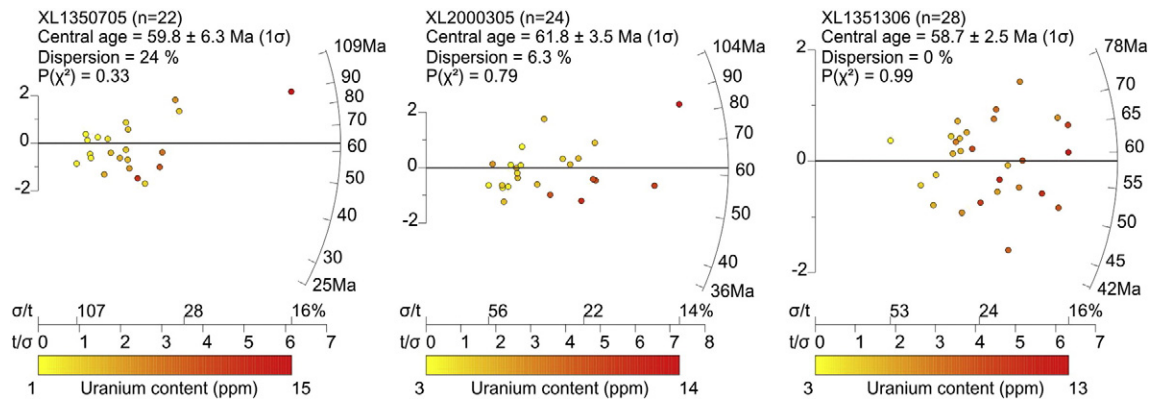| Sample number	Elevation (m)	Number of grains	ρ_d (N_d) ($\times 10^5$ cm^{-2})	ρ_s (N_s) ($\times 10^5$ cm^{-2})	ρ_i (N_i) ($\times 10^5$ cm^{-2})	Uranium content (ppm)	$P(\chi^2)$ (%)	Central Age (1σ, Ma)	Length (1σ, µm) (N)	Standard deviation (µm)
XL2000305	−200	24	9.585 (5967)	1.786 (459)	5.349 (1375)	7	79	61.8 ± 3.5	13.1 ± 0.4 (27)	2.0
XL1350705	−135	23	9.102 (5867)	1.331 (191)	3.770 (541)	6	33	59.8 ± 6.3	11.9 ± 0.4 (17)	1.8
XL1351306	−135	28	8.862 (5867)	1.975 (750)	5.776 (2194)	8	99	58.7 ± 2.5	12.3 ± 0.2 (112)	1.9

Fig. 9. Radial plots of apatite fission-track samples. The nearly horizontal lines in the radial plots represent the central AFT ages listed in Table 4.
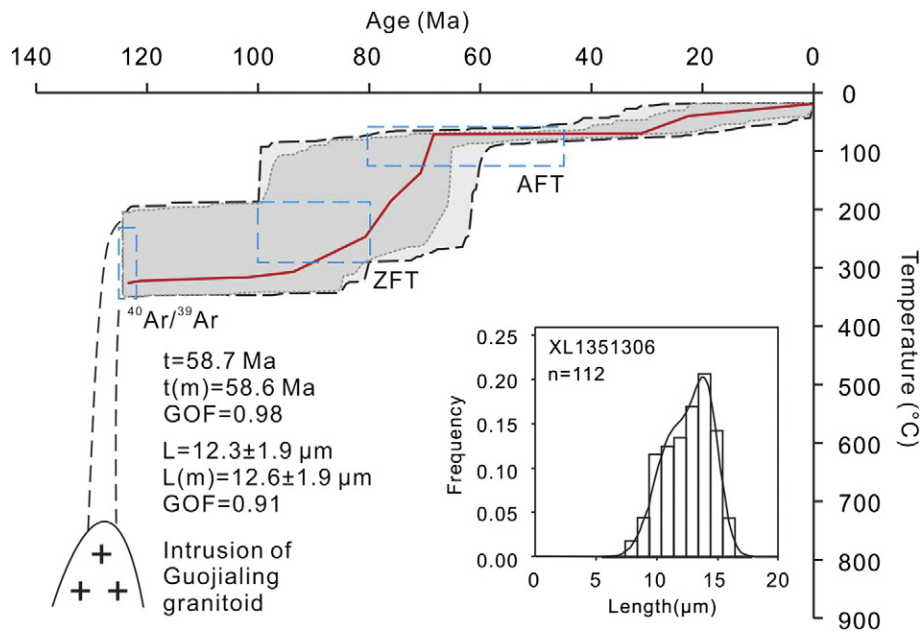

Fig. 10. Thermal history modelling of AFT results of sample XL1351306 using HeFTy software (Ketcham, 2012) and histogram of the apatite fission-track length distribution. Dark and light grey represent good and acceptable results, respectively, while the thick red line in the center of the dark grey means best-fit result. Blue dashed boxes represent time–temperature constraints during modelling. L, measured fission-track length; t, pooled AFT age; L(m), modelled fission-track length; t(m), modelled AFT age, n, track numbers. GOF represent the fitness between the modelled and measured values. Results with GOF >0.5 and >0.05 are considered good and acceptable, respectively. The timing and temperature of the intrusion of the Guojialing granitoid are from Wang et al. (1998), Zhang et al. (2010) and Yang et al. (2012).

to this shearing probably ceased before ~124 Ma, and lasted <4 million years.

Brittle normal faulting of the Sanshandao Fault and its subsidiary faults, which overprinted the pre-mineralization ductile shearing, increased the permeability of the gold-hosting rocks, resulting in the upwelling of the ore-forming fluids and enhanced fluid–rock interaction. The sealing of the permeable paths that may have accompanied this interaction, led to cycles of fracturing, fluid influx and sealing, fluid pressure increase and further fracturing. This resulted in large amounts of pyrite (Py_1 and Py_2; Fig. 4f, g) being deposited with minor gold, followed by a late generation of pyrite (Py_3) amalgamating clasts of early pyrite (Fig. 4f), and new fractures where base-metals and gold were

deposited (Fig. 4g). These geological features show that the fracturing and brecciation and fluid–rock interaction (Yang et al., 2016c) during normal faulting (Fig. 11b) were coupled, and played important roles in gold mineralization.
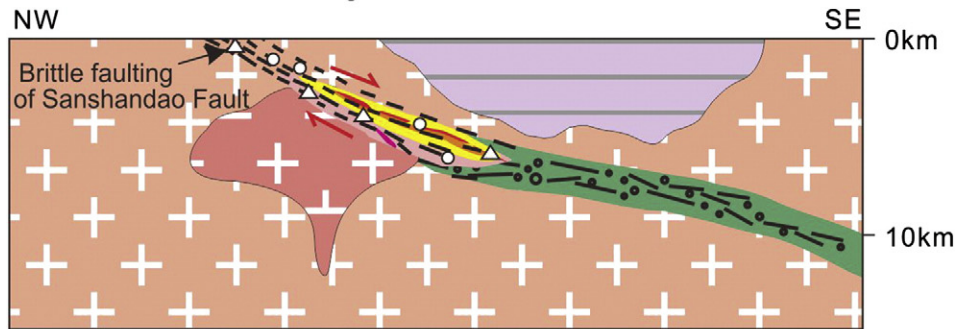
The best estimate for the timing of gold mineralization along the Sanshandao Fault is derived from a sericite $^{40}Ar/^{39}Ar$ age of ~121.3 ± 0.4 Ma (Zhang et al., 2003) from the Cangshang gold deposit. The sericite is demonstrably contemporaneous with the alteration, and sericite from all deposits along the neighbouring Jiaojia Fault yields a tight age group between 121 and 120 Ma (Li et al., 2003; Yang et al., 2016b). At the Xinli deposit, similar $^{40}Ar/^{39}Ar$ plateau ages were determined for the two fractured igneous K-feldspars at 121.5 ± 1.3 Ma and

Fig. 11. Cartoon showing the evolution of the Xinli gold deposit based on Fig. 10 and the main conclusions of this paper. (a) ~129 to 124 Ma, intrusion of Guojialing granitoid (Wang et al., 1998; Yang et al., 2012) and subsequent ductile shearing with cooling from ~800 to 400 °C during regional extension; (b) ~121 Ma determined by sericite ages and K-feldspar $^{40}Ar/^{39}Ar$ age resetting during the main phase of normal faulting, hydrothermal alteration, and gold mineralization (Zhang et al., 2003) between ~300 ± 50 °C and 240 ± 50 °C; (c) ~90 Ma, slight acceleration of cooling from 2 to 10–5 °C/Ma related to normal faulting and minor sinistral strike-slip movement of the regional Tan–Lu Fault (Wan and Zhu, 1996; Wang and Zhou, 2009; Wang et al., 2009); (d) ~60 Ma to present, slow cooling (1 °C/Ma) and exhumation (~125–60 °C–25 ± 5 °C) with the waning of movement on the Tan–Lu Fault (Wan et al., 1996).
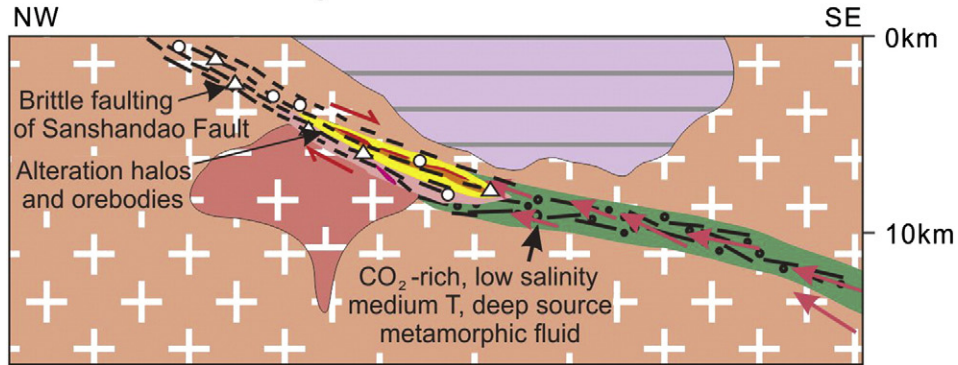
**d, ~60 Ma to present, relative slow cooling and exhumation from
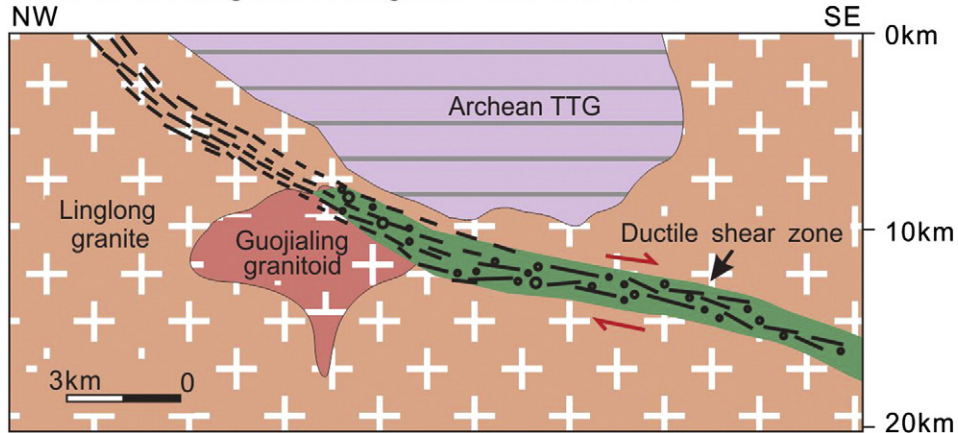~125-60°C to 25±5°C**
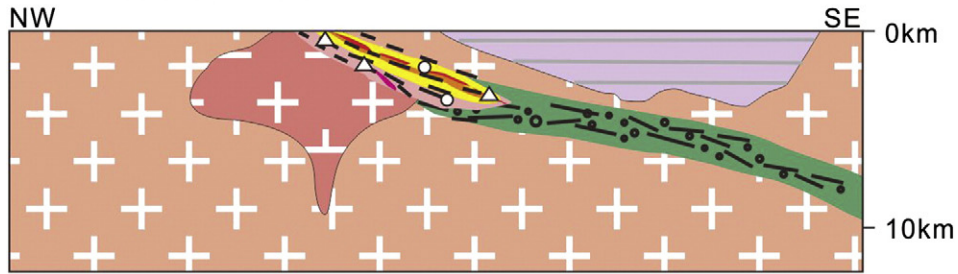
NW   SE
                                                         0km

                                                         10km

**c, ~90 Ma, slight acceleration of cooling from 2 to 10-5 °C/Ma
related to normal faulting**

NW   SE
                                                         0km

Brittle faulting
of Sanshandao Fault

                                                         10km

**b, ~121 Ma, hydrothermal alteration, gold mineralization and
related normal faulting between ~300±50°C and 240±50°C**

NW   SE
                                                         0km

Brittle faulting
of Sanshandao Fault

Alteration halos
and orebodies
                                                         10km

CO_2-rich, low salinity
medium T, deep source
metamorphic fluid

**a, ~129 to124 Ma, intrusion of Guojialing granitoid and subsequent
ductile shearing with cooling from ~800°C to 400°C**

NW   SE
                                                         0km

Archean TTG

Linglong   10km
granite   Guojialing
               granitoid   Ductile shear zone

3km   0
                                                         20km

120.5 ± 1.2 Ma. These are interpreted to represent the time of fracturing related to the intense normal faulting during gold mineralization and also the time of cooling within the mineralization temperature range of 300 ± 50 °C, and are younger than the $^{40}Ar/^{39}Ar$ plateau age of biotite of ~124 Ma (300 ± 50 °C) and older than the ZFT ages of ~90 Ma (240 ± 50 °C).

In summary, the intrusion of the Guojialing granitoid at ~129–128 Ma was followed by ductile shearing that pre-dated hydrothermal alteration, and finished before ~124 Ma. Large-scale hydrothermal alteration and gold mineralization occurred possibly at ~121 Ma as given by both sericite and K-feldspar $^{40}Ar/^{39}Ar$ plateau ages. Hydrothermal alteration and gold mineralization were controlled by normal faulting on the Sanshandao Fault which created the appropriate channelways to focus mineralizing fluids.

4.2. Cooling and exhumation of the Xinli deposit

The very rapid cooling of the Guojialing granitoid is indicated by the 4 million years time difference between its crystallization and reaching the closure temperature of biotite (300 ± 50 °C). This was followed by much slower cooling during the hydrothermal alteration and mineralization, as given by the time difference between the biotite cooling age of ~124 Ma and ZFT at ~90 Ma indicating temperatures of 240 ± 50 °C (Fig. 10). An estimate of the cooling rate during this period would be 60 °C/35 Ma or about 2 °C/Ma. The cooling rate accelerated slightly between ~90 Ma and ~70 Ma. Taking the range between 200 and 100 °C as the temperature difference between ~90 and ~70 Ma, the cooling rate is estimated at ~10–5 °C/Ma (Fig. 10). Afterwards, the deposit cooled to the present-day near-surface temperature (~25 ± 5 °C) at a rate of 1 °C/Ma (Figs. 10 and 11d).

Extension tectonics that gave rise to the regionally significant normal faults, such as the Linglong detachment and the Jiaojia Fault, and controlled mineralization, is thought to have evolved into a regional NW–SE compression event at ~120–110 Ma (Sun et al., 2007; Deng et al., 2015a) with evidence of change in subduction direction of the paleo-Pacific plate indicated by tracks of ocean island chains, stopping normal movement on these faults. The slight acceleration of cooling of the Xinli deposit around ~90 Ma (Figs. 10 and 11c) may relate to the normal reactivation of the Sanshandao Fault, which may have been caused by the normal faulting and minor sinistral strike-slip movement on the regional Tan–Lu Fault (Wan and Zhu, 1996; Wang and Zhou, 2009; Wang et al., 2009). This event has also been recorded by illite K–Ar ages of 86 ± 1 Ma and 68 ± 2 Ma for fault gouge of the adjoining Jiaojia Fault (Figs. 1 and 2; Deng et al., 2015a). Finally, movement on the regional Tan–Lu Fault weakened (Wan et al., 1996), and this area underwent relatively weak tectonic activity, slow cooling and exhumation until the present time (Figs. 10 and 11d). In summary, it is most probable that extension after mineralization at ~120 Ma was relatively minor associated with little topography, which has preserved the gold deposits in the northwestern part of the Jiaodong Peninsula.

5. Conclusions

At the Xinli gold deposit, on the footwall of the Sanshandao Fault, the gold-hosting Guojialing granitoid intruded at ~129–128 Ma. Subsequently, it underwent ductile shearing that ceased before ~124 Ma with rapid cooling from magmatic temperatures to 300 ± 50 °C. Mineralization was associated with subsequent brittle reactivation of normal movement of the Sanshandao Fault. Hydrothermal alteration and gold mineralization formed the Cangshan, Xinli and Sanshandao deposits, and offshore resources to the north of the Sanshandao deposit, altogether with 760 t of contained Au, along the Sanshandao Fault at ~121 Ma as estimated from a published sericite $^{40}Ar/^{39}Ar$ age (Zhang et al., 2003). At the Xinli deposit, the fractured igneous K-feldspar $^{40}Ar/^{39}Ar$ ages of ~121 Ma record closely the time of normal faulting, which created the channelways for the mineralizing fluids, and cooling within the range

of mineralization temperature of 300 ± 50 °C. After gold mineralization, the deposit cooled slowly to 240 ± 50 °C at ~90 Ma at a cooling rate of ~2 °C/Ma, with a period of faster cooling at a rate up to 10 °C/Ma, probably due to reactivation of movement on the Sanshandao Fault at ~90–70 Ma contemporaneous with reactivation of the first order Tan Lu Fault. Then, from ~70 Ma to the present, the deposit cooled at an average cooling rate of ~1 °C/Ma. Weak topography and little post-mineralization exhumation resulted from extension and normal faulting preserved the deposit.

References

Bernet, M., 2009. A field-based estimate of the zircon fission-track closure temperature. Chem. Geol. 259, 181–189.

Betsi, T.B., Lentz, D., McInnes, B., Evans, N.J., 2012. Emplacement ages and exhumation rates for intrusion-hosted Cu-Mo-Sb-Au mineral systems at Freegold Mountain (Yukon Canada): assessment from U-Pb, Ar-Ar and (U-Th)/He geochronometers. Can. J. Earth Sci. 49, 653–670.

Charles, N., Gumiaux, C., Augier, R., Chen, Y., Zhu, R.X., Lin, W., 2011. Metamorphic core complexes vs. synkinematic plutons in continental extension setting: insights from key structures (Shandong Province, eastern China). J. Asian Earth Sci. 40, 261–278.

Charles, N., Augier, R., Gumiaux, C., Monié, P., Chen, Y., Faure, M., Zhu, R.X., 2013. Timing, duration and role of magmatism in wide rift systems: insights from the Jiaodong Peninsula (China, East Asia). Gondwana Res. 24, 412–428.

Deng, J., Wang, Q.F., 2016. Gold mineralization in China: metallogenic provinces, deposit types and tectonic framework. Gondwana Res. 36, 219–274.

Deng, J., Wang, Q.F., Wan, L., Liu, H., Yang, L.Q., Zhang, J., 2011. A multifractal analysis of mineralization characteristics of the Dayingezhuang disseminated-veinlet gold deposit in the Jiaodong gold province of China. Ore Geol. Rev. 40, 54–64.

Deng, J., Yuan, W.M., Emmanuel, J.M.C., Yang, L.Q., Wang, C.M., Yang, L.Y., Hao, N.N., 2014. Geochronology and thermochronometry of the Jiapigou gold belt, northeastern China: new evidence for multiple episodes of mineralization. J. Asian Earth Sci. 89, 10–27.

Deng, J., Wang, C.M., Bagas, L., Carranza, E.J.M., Lu, Y.J., 2015a. Cretaceous–Cenozoic tectonic history of the Jiaojia Fault and gold mineralization in the Jiaodong Peninsula, China: constraints from zircon U–Pb, illite K–Ar, and apatite fission track thermochronometry. Mineral Deposits 50, 987–1006.

Deng, J., Liu, X.F., Wang, Q.F., Pan, R.G., 2015b. Origin of the Jiaodong-type Xinli gold deposit, Jiaodong Peninsula, China: Constraints from fluid inclusion and C–D–O–S–Sr isotope compositions. Ore Geol. Rev. 65, 674–686.

Forster, M.A., Lister, G.S., 2004. The interpretation of $^{40}Ar/^{39}Ar$ apparent age spectra produced by mixing: application of the method of asymptotes and limits. J. Struct. Geol. 26, 287–305.

Fu, Y.L., Lu, X.Q., Zhang, S.H., Wang, L.T., 1987. $^{40}Ar/^{39}Ar$ dating techniques and age determination of some geological samples. Bull. Inst. Géol. 17, 85–107 (in Chinese with English abstract).

Galbraith, R.F., 1981. On statistical models for fission track counts. Math. Geol. 13, 471–483.

Galbraith, R.F., 1984. On statistical estimation in fission track dating. J. Int. Assoc. Math. Geol. 16, 653–669.

Gleadow, A.J.W., 1981. Fission-track dating method: what are the real alternatives? Nucl. Track Detect. 2, 105–117.

Gleadow, A.J.W., Duddy, I.R., 1981. A natural long-term track annealing experiment for apatite. Nucl. Tracks 5, 169–174.

Goldfarb, R.J., Santosh, M., 2014. The dilemma of the Jiaodong gold deposits: are they unique? Geosci. Front. 5 (2), 139–153.

Goss, S.C., Wilde, S.A., Wu, F., Yang, J., 2010. The age, isotopic signature and significance of the youngest Mesozoic granitoids in the Jiaodong Terrane, Shandong Province, North China Craton. Lithos 3, 309–326.

Groves, D.I., Santosh, M., 2016. The giant Jiaodong gold province: the key to a unified model for orogenic gold deposits? Geosci. Front. 7, 409–417.

Groves, D.I., Goldfarb, R.J., Gebre-Mariam, M., Hagemann, S.G., Robert, F., 1998. Orogenic gold deposits: a proposed classification in the context of their crustal distribution and relationship to other gold deposit types. Ore Geol. Rev. 13, 7–27.

Hurford, A.J., 1986. Cooling and uplift patterns in the Lepontine Alps South Central Switzerland and an age of vertical movement on the Insubric fault line. Contrib. Mineral. Petrol. 92, 413–427.

Hurford, A.J., Green, P.F., 1983. The zeta age calibration of fission-track dating. Isot. Geosci. 1, 285–317.

Ketcham, R.A., 2012. User's manual for HeFTy version 1.7.5.

Ketcham, R.A., Carter, A.C., Donelick, R.A., Barbarand, J., Hurford, A.J., 2007. Improved measurement of fission-track annealing in apatite using c-axis projection. Am. Mineral. 92, 789–798.

Lanphere, M.A., Baadsgaard, H., 2001. Precise K–Ar, ^{40}Ar/^{39}Ar, Rb–Sr and U/Pb mineral ages from the 27.5 Ma Fish Canyon Tuff reference standard. Chem. Geol. 175, 653–671.

Li, J.W., Vasconcelos, P.M., Zhang, J., Zhou, M.F., Zhang, X.J., Yang, F.H., 2003. ^{40}Ar/^{39}Ar constraints on a temporal link between gold mineralization, magmatism, and continental margin transtension in the Jiaodong gold province, eastern China. J. Geol. 111, 741–751.

Li, X.C., Fan, H.R., Santosh, M., Hu, F.F., Yang, K.F., Lan, T.G., Liu, Y.S., Yang, Y.H., 2012. An evolving magma chamber within extending lithosphere: an integrated geochemical isotopic and zircon U–Pb geochronological study of the Gushan granite eastern North China Craton. J. Asian Earth Sci. 50, 27–43.

Li, L., Santosh, M., Li, S.R., 2015. The 'Jiaodong type' gold deposits: characteristics, origin and prospecting. Ore Geol. Rev. 65, 589–611.

Liu, Z.J., 2010. Post-ore Denudation and Exploration Potential of the Northwestern Jiaodong Gold Province, China Dissertation China University of Geoscience, Beijing.

Liu, Z.J., Wang, J.P., Zheng, D.W., Liu, J.J., Liu, J., Fu, C., 2010. Exploration prospect and post-ore denudation in the northwestern Jiaodong gold province, China: evidence from apatite fission track thermochronology. Acta Petrol. Sin. 26, 3597–3611 (in Chinese with English abstract).

Liu, Y., Deng, J., Wang, Z.L., Zhang, L., Zhang, C., Liu, X.D., Zheng, X.L., Wang, X.D., 2014. Zircon U–Pb age, Lu-Hf isotopes and petrogeochemistry of the monzogranites from Xincheng gold deposit, northwestern Jiaodong Peninsula, China. Acta Petrol. Sin. 30, 2559–2573 (in Chinese with English abstract).

Ludwig, K.R., 2012. User's manual for Isoplot 4.16: a geochronological toolkit for Microsoft Excel.

Ma, L., Jiang, S.Y., Dai, B.Z., Jiang, Y.H., Hou, M.L., Pu, W., Xu, B., 2013. Multiple sources for the origin of Late Jurassic Linglong adakitic granite in the Shandong Peninsula, eastern China: zircon U–Pb geochronological, geochemical and Sr-Nd-Hf isotopic evidence. Lithos 162, 175–194.

Márton, I., Moritz, R., Spikings, R., 2010. Application of low-temperature thermochronology to hydrothermal ore deposits: formation preservation and exhumation of epithermal gold systems from the eastern Rhodopes Bulgaria. Tectonophysics 483, 240–254.

McDougall, I., Harrison, T.M., 1999. Geochronology and Thermochronology by the ^{40}Ar/^{39}Ar Method. Oxford University Press, Oxford.

McInnes, B.I.A., Noreen, J.E., Fu, F.Q., Steve, G., 2005. Application of thermochronology to hydrothermal ore deposits. Rev. Mineral. Geochem. 58, 467–498.

Nier, A.O., 1950. A redetermination of the relative abundances of the isotopes of carbon, nitrogen, oxygen, argon, and potassium. Phys. Rev. 77, 789.

Pan, R.G., 2013. Evolution of Ore-forming Fluids of Xinli Gold Deposit, Jiaodong Peninsula, Eastern China Dissertation China University of Geosciences, Beijing (in Chinese with English abstract).

Passchier, C.W., Trouw, R.A., 2005. Microtectonics. 2nd ed. Springer, Heidelberg.

Phillips, G.N., Powell, R., 2015. A practical classification of gold deposits with a theoretical basis. Ore Geol. Rev. 65, 568–573.

Qiu, Y., Groves, D.I., McNaughton, N.J., Wang, L.G., Zhou, T., 2002. Nature, age, and tectonic setting of granitoid-hosted, orogenic gold deposits of the Jiaodong Peninsula, eastern North China craton. China. Miner. Dep. 37 (3–4), 283–305.

Reddy, S.M., Potts, G.J., Kelley, S.P., Arnaud, N.O., 1999. The effects of deformation-induced microstructures on intragrain ^{40}Ar/^{39}Ar ages in potassium feldspar. Geology 27, 363–366.

Reiners, P.W., Ehlers, T.A., 2005. In: Reiners, P.W., Ehlers, T.A. (Eds.), Low-Temperature Thermochronology: Techniques, Interpretations, and Applications. The Miner. Soc. of America, Washington.

Reiners, P.W., Ehlers, T.A., Zeitler, P.K., 2005. Past, present, and future of thermochronology. Rev. Mineral. Geochem. 58, 1–18.

Song, M.C., Li, S.Z., Santosh, M., Zhao, S., Yu, S., Yi, P.H., Cui, S.X., Lv, G.X., Xu, J.X., Song, Y.X., Zhou, M.L., 2015a. Types, characteristics and metallogenesis of gold deposits in the Jiaodong Peninsula, Eastern North China Craton. Ore Geol. Rev. 65, 612–625.

Song, M.C., Zhang, J.J., Zhang, P.J., Yang, L.Q., Liu, D.H., Ding, Z.J., Song, Y.X., 2015b. Discovery and tectonic-magmatic background of superlarge gold deposit in offshore of northern Sanshandao, Shandong Peninsula, China. Acta Petrol. Sin. 89, 365–383 (in Chinese with English abstract).

Steiger, R.H., Jäger, E., 1977. Subcommission on geochronology: convention on the use of decay constants in geo-and cosmochronology. Earth Planet. Sci. Lett. 36, 359–362.

Sun, W.D., Ding, X., Hu, Y.H., Li, X.H., 2007. The golden transformation of the Cretaceous plate subduction in the West Pacific. Earth Planet. Sci. Lett. 262, 533–542.

Sun, H.S., Han, J.B., Shen, Y.K., Liu, L., Leng, S.L., Xu, C., Yang, Q.M., Ge, F.J., Ouyang, S.B., Deng, X., 2016. Zircon (U-Th)/He age and its implication for post-mineralization exhumation degree of Linglong and Jiaojia goldfields, northwest Jiaodong, China. Earth Sci. 41, 644–654 (in Chinese with English abstract).

Vermeesch, P., 2009. RadialPlotter: a Java application for fission track, luminescence and other radial plots. Radiat. Meas. 44, 409–410.

Wagner, G., Haute, P.V.D., 1992. Fission-track Dating. Springer Science & Business Media.

Wan, T.F., Zhu, H., 1996. The maximum sinistral strike-slip and its forming stage for the Tancheng–Lujiang Fault Zone. In: Zhao, Y.H. (Ed.), Formation and Evolution of the Tancheng–Lujiang Fault Zone. China University Geosciences Press, Beijing, pp. 56–69 (in Chinese).

Wan, T.F., Zhu, H., Zhao, L., Lin, J.P., Cheng, J., Chen, J., 1996. Formation and evolution of the Tancheng-Lujiang Fault Zone: a review. J. Grad. Sch. China Univ. Geosci. 10, 159–168 (in Chinese with English abstract).

Wang, S.N., 1983. Age determinations of ^{40}Ar-^{40}K, ^{40}Ar-^{39}Ar and radiogenic ^{40}Ar released characteristics on K-Ar geostandards of China. Sci. Geol. Sin. 4, 315–323 (in Chinese with English abstract).

Wang, Y., Li, H.M., 2008. Initial formation and Mesozoic tectonic exhumation of an intracontinental tectonic belt of the northern part of the Taihang Mountain belt, eastern Asia. J. Geol. 116, 155–172.

Wang, Y., Zhou, S., 2009. ^{40}Ar/^{39}Ar dating constraints on the high-angle normal faulting along the southern segment of the Tan-Lu fault system: an implication for the onset of eastern China rift-systems. J. Asian Earth Sci. 34, 51–60.

Wang, L.G., Qiu, Y.M., McNaughton, N.J., Groves, D.I., Luo, Z.K., Huang, J.Z., Miao, L.C., Liu, Y.K., 1998. Constraints on crustal evolution and gold metallogeny in the northwestern Jiaodong Peninsula, China, from SHRIMP U-Pb zircon studies of granitoids. Ore Geol. Rev. 13, 275–291.

Wang, Y.S., Zhu, G., Hu, Z.Q., Zhang, B.L., Xiang, B.W., Xie, C.L., 2009. K-Ar dating of extensional fault gouge from the Yi-Shu segment of the Tan-Lu fault zone. Sci. China Ser. D Earth Sci. 52, 489–503.

Wang, Z.L., Yang, L.Q., Deng, J., Santosh, M., Zhang, H.F., Liu, Y., Li, R.H., Huang, T., Zheng, X.L., Zhao, H., 2014. Gold-hosting high Ba-Sr granitoids in the Xincheng gold deposit, Jiaodong Peninsula, East China: petrogenesis and tectonic setting. J. Asian Earth Sci. 95, 274–299.

Wang, Z.L., Yang, L.Q., Guo, L.N., Marsh, E., Wang, J.P., Liu, Y., Zhang, C., Li, R.H., Zhang, L., Zheng, X.L., Zhao, R.X., 2015. Fluid immiscibility and gold deposition in the Xincheng deposit, Jiaodong Peninsula, China: a fluid inclusion study. Ore Geol. Rev. 65, 701–707.

Wang, Y., Zwingmann, H., Zhou, L., Lo, C.H., Viola, G., Hao, J., 2016. Direct dating of folding events by ^{40}Ar/^{39}Ar analysis of synkinematic muscovite from flexural-slip planes. J. Struct. Geol. 83, 46–59.

Wei, W.S., Mu, T., Zhang, H.H., 2001. Geological Map of Jiaodong Gold Province Showing the Metallogenic Belts, Ore Deposit Types and Distribution of the Gold Deposits. Gold Geology Research Institute of China Armed Police Force, Lang Fang, Hebei.

Wu, F.Y., Xu, Y.G., Gao, S., Zheng, J.P., 2008. Lithospheric thinning and destruction of the North China Craton. Acta Petrol. Sin. 24, 1145–1174 (in Chinese with English abstract).

Yang, K.F., Fan, H.R., Santosh, M., Hu, F.F., Wilde, S.A., Lan, T.G., Liu, Y.S., 2012. Reactivation of the Archean lower crust: implications for zircon geochronology, elemental and Sr-Nd-Hf isotopic geochemistry of late Mesozoic granitoids from northwestern Jiaodong Terrane, the North China Craton. Lithos 146, 112–127.

Yang, L.Q., Deng, J., Wang, Z.L., Zhang, L., Guo, L.N., Song, M.C., Zheng, X.L., 2014a. Mesozoic gold metallogenic system of the Jiaodong gold province, eastern China. Acta Petrol. Sin. 30, 2447–2467 (in Chinese with English abstract).

Yang, Q.Y., Santosh, M., Shen, J.F., Li, S.R., 2014b. Juvenile vs recycled crust in NE China: zircon U–Pb geochronology Hf isotope and an integrated model for Mesozoic gold mineralization in the Jiaodong Peninsula. Gondwana Res. 25, 1445–1468.

Yang, L.Q., Deng, J., Goldfarb, R.J., Zhang, J., Gao, B.F., Wang, Z.L., 2014c. ^{40}Ar/^{39}Ar geochronological constraints on the formation of the Dayingezhuang gold deposit: new implications for timing and duration of hydrothermal activity in the Jiaodong gold province, China. Gondwana Res. 25, 1469–1483.

Yang, L.Q., Deng, J., Wang, Z.L., Zhang, L., Goldfarb, R.J., Yuan, W.M., Weinberg, R.F., Zhang, R.Z., 2016a. Thermochronologic constraints on evolution of the Linglong Metamorphic Core Complex and implications for gold mineralization: a case study from the Xiadian gold deposit Jiaodong Peninsula eastern China. Ore Geol. Rev. 72, 165–178.

Yang, L.Q., Guo, L.N., Wang, Z.L., Zhao, R.X., Song, M.C., Zheng, X.L., 2016b. Timing and mechanism of gold mineralization at the Wang'ershan gold deposit, Jiaodong Peninsula, eastern China. Ore Geol. Rev. http://dx.doi.org/10.1016/j.oregeorev.2016.06.027.

Yang, L.Q., Deng, J., Wang, Z.L., Guo, L.N., Li, R.H., Groves, D.I., Danyushevskiy, L., Zhang, C., Zheng, X.L., Zhao, H., 2016c. Relationships between gold and pyrite at the Xincheng gold deposit Jiaodong Peninsula China: implications for gold source and deposition in a brittle epizonal environment. Econ. Geol. 111, 105–126.

Yuan, W.M., Zheng, Q.G., Bao, Z.K., Dong, J.Q., Carter, A., An, Y.C., Deng, J., 2009. Zircon fission track thermochronology constraints on mineralization epochs in Altai Mountains, northern Xinjiang, China. Radiat. Meas. 44, 950–954.

Zaun, P.E., Santosh, G.A., 1985. Fission-track stability in zircons under geological conditions. Nucl. Tracks Radiat. Meas. 10, 303–307.

Zhang, X.O., Cawood, P.A., Wilde, S.A., Liu, R.Q., Song, H.L., Li, W., Snee, L.W., 2003. Geology and timing of mineralization at the Cangshang gold deposit, Northwestern Jiaodong Peninsula, China. Mineral Deposits 38, 141–153.

Zhang, J., Zhao, Z.F., Zheng, Y.F., Dai, M., 2010. Postcollisional magmatism: geochemical constraints on the petrogenesis of Mesozoic granitoids in the Sulu orogen China. Lithos 119, 512–536.

Zhang, L., Wang, Z.L., Li, G.W., Zheng, X.L., An, P., Chen, B.Y., 2016. ^{40}Ar/^{39}Ar and fission-track dating constraints on the tectonothermal history of the world-class Sanshandao gold deposit, Jiaodong peninsula, eastern China. Acta Petrol. Sin. 32, 2465–2476 (in Chinese with English abstract).